Estimation of dynamic petrophysical properties of water-bearing sands invaded with oil-base mud from the interpretation of multiple borehole geophysical measurements

Zoya Heidari[1] and Carlos Torres-Verdín[2]

ABSTRACT

Nonmiscible fluid displacement without salt exchange takes place when oil-base mud (OBM) invades connate water-saturated rocks. This is a favorable condition for the estimation of dynamic petrophysical properties, including saturation-dependent capillary pressure. We developed and successfully tested a new method to estimate porosity, fluid saturation, permeability, capillary pressure, and relative permeability of water-bearing sands invaded with OBM from multiple borehole geophysical measurements. The estimation method simulates the process of mud-filtrate invasion to calculate the corresponding radial distribution of water saturation. Porosity, permeability, capillary pressure, and relative permeability are iteratively adjusted in the simulation of invasion until density, photoelectric factor, neutron porosity, and apparent resistivity logs are accurately reproduced with numerical simulations that honor the postinvasion radial distribution of water saturation. Examples of application include oil- and gas-bearing reservoirs that exhibit a complete capillary fluid transition between water at the bottom and hydrocarbon at irreducible water saturation at the top. We show that the estimated dynamic petrophysical properties in the water-bearing portion of the reservoir are in agreement with vertical variations of water saturation above the free water-hydrocarbon contact, thereby validating our estimation method. Additionally, it is shown that the radial distribution of water saturation inferred from apparent resistivity and nuclear logs can be used for fluid-substitution analysis of acoustic compressional and shear logs.

INTRODUCTION

Conventional well-log interpretation often resorts to water-bearing reservoir units to estimate connate-water electrical resistivity based on the relationship between formation porosity and electrical resistivity (Pickett, 1966). However, in the case of nonnegligible invasion with water-base mud (WBM) filtrate, it is necessary to account for the effect of salt mixing between connate water and mud filtrate when estimating connate-water resistivity. Such interpretation methods can be unreliable in the presence of residual hydrocarbon saturation because the water saturation sensed by apparent resistivity logs remains unknown. Conversely, in the case of invasion with oil-base mud (OBM), the invasion process involves immiscible fluid displacement between OBM-filtrate and water, whereby no change in water salinity takes place. This relatively favorable condition opens the possibility of reliable estimation of dynamic petrophysical properties of the invaded rock formation from the estimation of the radial distribution of water saturation. To date, no petrophysical interpretation method has been advanced to take advantage of the immiscibility between OBM-filtrate and connate water to estimate fundamental dynamic properties of rock formations such as permeability, capillary pressure, and relative permeability.

Recent publications emphasize the importance of numerical simulation of well logs to estimate static and dynamic petrophysical properties of rock formations (Salazar et al., 2006; Malik et al., 2008; Heidari et al., 2011; Salazar et al., 2011). One of the technical challenges inherent to these studies is the nonuniqueness of the estimation due to the large number of unknown petrophysical properties. A way to approach the solution is to use core data as external

information. To overcome the problem of nonuniqueness in the estimation, the interpretation method advanced in this paper invokes multiple borehole geophysical measurements and is based on the numerical simulation of gamma ray (GR), photoelectric factor (PEF), electrical resistivity, neutron porosity, and density logs from the postinvasion radial distribution of fluid saturation resulting from invasion.

Depending on the dynamic petrophysical properties of the formation — notably permeability, capillary pressure, and relative permeability — the displacement of water with OBM-filtrate will result in shallow, deep, sharp, and/or spatially smooth radial fronts of water saturation away from the borehole wall. The corresponding effect on electrical resistivity measurements with variable radial lengths of investigation will be either "stacked" or "separated" apparent resistivity logs. Because of the relatively low values of formation electrical resistivity in this specific case of analysis (water-bearing sands and salty connate water), induction electrical resistivity logs will exhibit measurable sensitivity to radial variations of water saturation away from the borehole wall (recall that induction resistivity measurements remain sensitive to variations of electrical conductivity, i.e., the inverse of electrical resistivity).

The interpretation method described in this paper assumes a vertical well, horizontal layers, and axial symmetric invasion. It is initialized with the construction of a multilayer petrophysical model. Layer-by-layer properties are populated with results obtained from conventional petrophysical interpretation of well logs. The process of mud-filtrate invasion is numerically simulated in permeable layers assuming no hydraulic communication between adjacent beds. Subsequently, apparent resistivity and nuclear logs are numerically simulated from the radial distribution of water saturation obtained from the simulation of mud-filtrate invasion (nuclear logs are simulated using a recently developed fast linear iterative refinement method [Mendoza et al., 2010]). We iteratively adjust the initial guess of layer-by-layer petrophysical properties to minimize the difference between well logs and their numerical simulations, thereby rendering final estimates of static and dynamic petrophysical properties.

The procedure is first implemented in pure-shale zones (which are not normally affected by mud-filtrate invasion) to estimate shale porosity, volumetric concentration of clay, and bound-water resistivity. Estimated properties from this first step are assumed equal to those of shale encountered in water-saturated zones to estimate nonshale porosity, absolute permeability, and saturation-dependent capillary pressure and relative permeability. Estimated properties are thereafter used in hydrocarbon-bearing zones to quantify hydrocarbon pore volume. The overall interpretation procedure is verified by correlating the saturation-dependent capillary pressure estimated in water-bearing sands with that of vertical variations of water saturation due to capillary equilibrium in a hydrocarbon reservoir underlain by an active aquifer.

The following sections detail the implementation, application, and limitations of the new interpretation method introduced in this paper. To verify the reliability and accuracy of results in capillary transition zones, we consider three
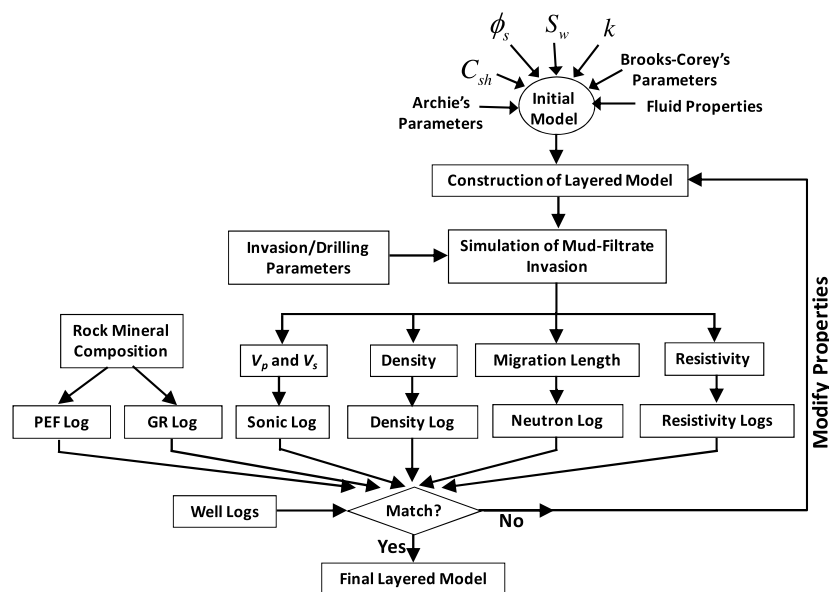

Figure 1. Iterative workflow adopted to estimate unknown petrophysical properties. Nonlinear iterations are intended to progressively improve the agreement between measured and numerically simulated electrical resistivity and nuclear well logs with the adjustment of petrophysical properties.

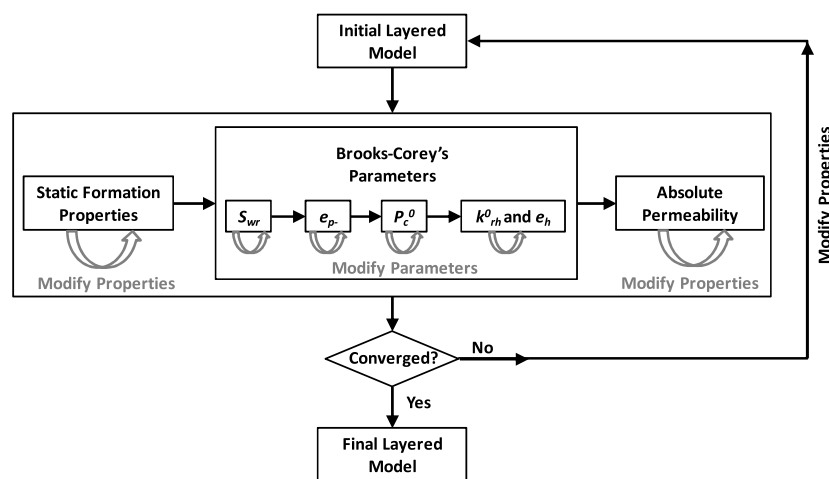Figure 2. Iterative serial inversion loops adopted to estimate layer-by-layer static petrophysical properties (porosity, volumetric concentration of shale, and initial water saturation), Brooks-Corey's parameters, and absolute permeability. Each group of properties is updated in serial inversion loops assuming that remaining groups are fixed. This process continues iteratively until achieving convergence.

challenging examples of application that include hydrocarbon-bearing formations underlain by active aquifers. Field examples cover a wide range of porosity and permeability values in various siliciclastic sedimentary sequences.

METHOD

Combined iterative numerical simulation of well logs to estimate petrophysical properties

Estimation of petrophysical properties is performed with a combined simulation algorithm that iteratively updates unknown properties by reducing the difference between well logs and their numerical simulations. The first step is to construct a layered model and generate an initial guess for static and dynamic petrophysical properties in the identified petrophysical layers of the multilayer formation. Secondly, we numerically simulate the process of mud-filtrate invasion to determine the radial distribution of water saturation in the near-wellbore region of each layer. The next step numerically simulates nuclear and apparent resistivity logs and compares them to available well logs. We then iteratively update the initial guess of layer-by-layer properties to reduce the difference between measurements and simulations. Figure 1 is a flowchart of the implemented procedure for combined iterative numerical simulation and automatic inversion of well logs to estimate porosity, water saturation, volumetric concentration of shale, permeability, saturation-dependent capillary pressure, and relative permeability.

To expedite the estimation process, we begin with the assessment of porosity and volumetric concentration of shale. Next, we approximate irreducible water saturation (i.e., the water saturation at which the relative permeability to water becomes zero) and initial water saturation by matching deep and shallow apparent resistivity logs with their numerical simulations. The last step is to estimate permeability and Brooks-Corey's parameters of saturation-dependent capillary pressure and relative permeability by matching the separation of apparent resistivity logs. After the first pass, we return to the assessment of porosity and update all the parameters to secure a good agreement between well logs and their numerical simulations (Figure 2). There could be more than one solution for each petrophysical property depending on the availability of core measurements, sensitivity of well logs to every unknown parameter, and number of unknown properties. Sensitivity analysis is recommended to quantify (1) the range of sensitivity of available well logs to unknown petrophysical properties, and (2) the expected uncertainty range for estimated properties in different formations. The following sections briefly explain the assumed rock model and every step of the estimation procedure.

Petrophysical analysis and construction of an initial guess

Conventional well-log interpretation is used to generate an initial guess for layer-by-layer values of porosity, fluid saturation, volumetric concentration of shale, and permeability. We use neutron porosity and density logs to calculate porosity. Shaly sand resistivity models (e.g., dual water model [Clavier et al., 1977]) are invoked to

estimate water saturation. Volumetric concentration of shale is estimated based on GR, density, and neutron porosity logs. The initial guess for permeability is obtained with Timur's formula (Timur, 1968). Bed boundaries are detected based on inflection points of GR, PEF, and density logs. The initial guess for layer-by-layer petrophysical properties is the average of log-calculated properties between detected bed boundaries.

Table 1. Trinidad Shaly Sand, Field Example No. 3: Summary of assumed Archie's parameters and matrix, mud, fluid, and formation properties.

Variable	Value	Units
Archie's factor, a	1.00	–
Archie's porosity exponent, m	1.72	–
Archie's saturation exponent, n	1.89	–
Connate-water resistivity at 133°F	0.07	ohm-m
Bound-water resistivity at 133°F	0.03	ohm-m
Water density	1.00	g/cm^3
Water viscosity	1.00	cp
In situ hydrocarbon density	0.65	g/cm^3
Hydrocarbon viscosity	1.0	cp
Mud-filtrate density	0.8	g/cm^3
Mud-filtrate viscosity	1.5	cp
Formation temperature	133.0	°F
Initial formation pressure	67.57	MPa
Mudcake reference permeability	0.03	mD
Mudcake reference porosity	0.30	–
Mud solid fraction	0.06	–
Mudcake maximum thickness	1.02	cm
Mudcake compressibility exponent	0.40	–
Mudcake exponent multiplier	0.10	–
Wellbore radius	18.42	cm
Shale porosity	0.05	–
Overbalance pressure	0.69	MPa
Formation maximum invasion time	3.0	days

Table 2. Synthetic Case No. 1, inversion of single parameters assuming that remaining parameters are fixed: assumed model properties, initial guess, estimated properties and corresponding uncertainty range for properties estimated after perturbing well logs with zero-mean, 2% random Gaussian additive noise. Figure 14 shows the capillary pressure curve associated with these parameters.

Parameter	Model	Initial	Final estimate	Uncertainty range
P_c^0 (MPa.Darcy$^{1/2}$)	0.186	0.165	0.186	0.179–0.249
e_p	5.0	4.0	5.0	4.5–5.5
k_{rh}^0	0.7	0.8	0.7	0.4–0.9
e_h	2.5	4	2.5	2–3.1
k (mD)	400.0	450.0	400.0	130–530

Rock model

   The rock model assumed in this paper consists of matrix, shale, and nonshale porosity that includes water and hydrocarbon. Water and hydrocarbon can be movable or residual. Shale is assumed to be of the dispersed type (Poupon et al., 1970). Even though the specific application considered in this paper assumes dispersed shale, the formulation can be easily modified to account for the case of laminated or structural shale.

   The relationship among the volumetric concentrations of all rock components is expressed as (Mezzatesta et al., 2006):

$$\sum_{i=1}^{n_c} C_i + C_{sh} + \phi_s = 1, \qquad (1)$$

where C_i is volumetric concentration of the assumed mineral constituents in the matrix, C_{sh} is volumetric concentration of shale, ϕ_s is nonshale porosity, and n_c is the number of mineral constituents. Volumetric concentration of shale is defined as:

$$C_{sh} = \frac{V_{sh}}{V_r}, \qquad (2)$$

where V_r is rock volume including fluids and V_{sh} is volume of wet shale. We calculate bulk density (ρ_b) via the following equation:

$$\rho_b = \sum_{i=1}^{n_c} (C_i \rho_i) + \rho_f \phi_s + \rho_{sh} C_{sh}, \qquad (3)$$

where ρ_i is density of the corresponding mineral, ρ_f is fluid density, and ρ_{sh} is shale density. Wet shale consists of clay and silt, which includes clay-bound water. Fluid density and shale density are given by

Table 3. Synthetic Case No. 1, iterative serial loop inversion of all unknown properties: Assumed model properties, initial guess, final estimates (after the second iteration of inversion), and corresponding uncertainty range for properties estimated after perturbing well logs with zero-mean, 2% random Gaussian additive noise. Figure 14 shows the capillary pressure curve associated with these parameters.

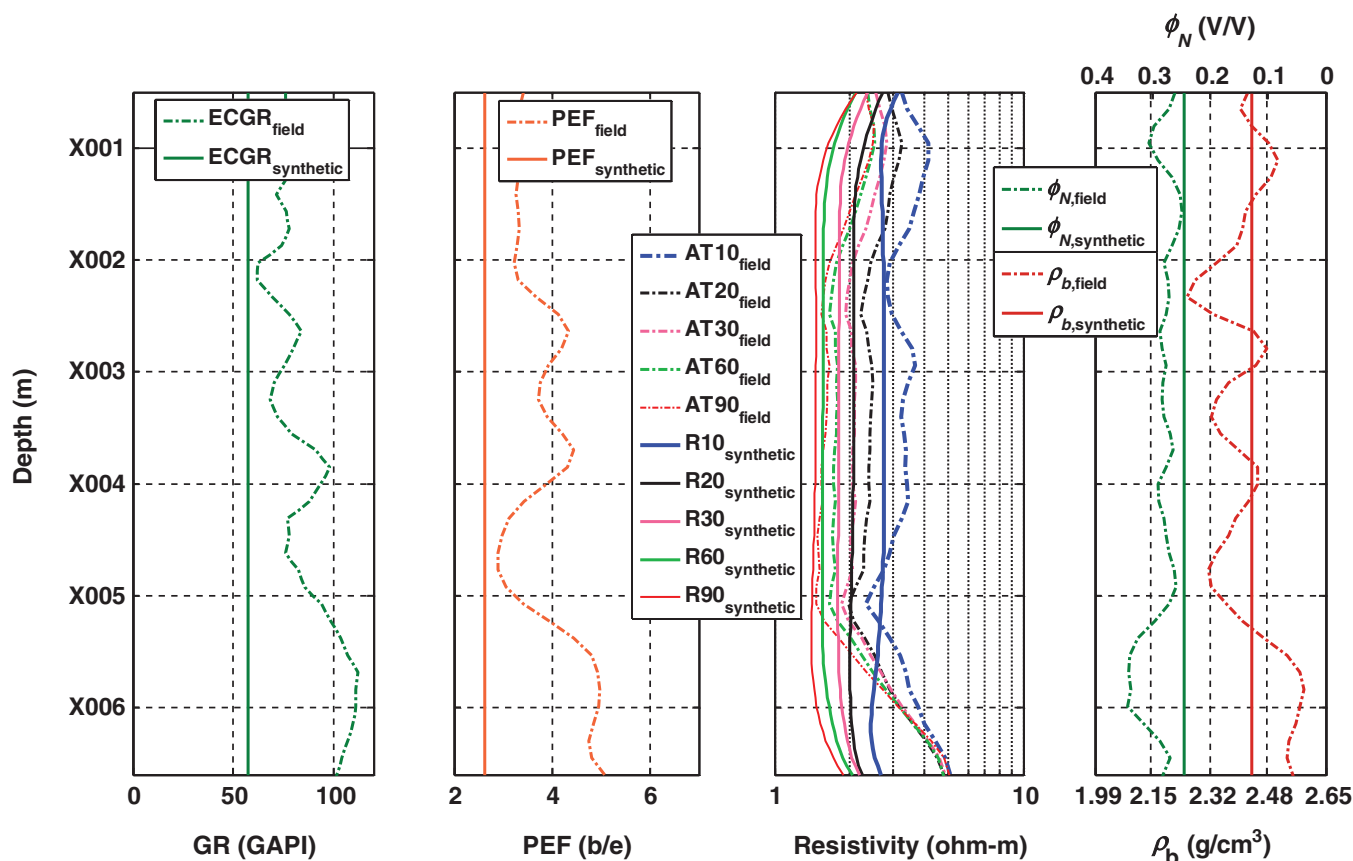| Parameter	Model	Initial	Final estimate	Uncertainty range
P_c^0 (MPa.Darcy$^{1/2}$)	0.186	0.165	0.205	0.198–0.266
e_p	5.0	4.0	4.6	4.1–5.1
k_{rh}^0	0.7	0.8	0.75	0.50–0.98
e_h	2.5	4.0	2.7	2.2–3.2
k (mD)	400.0	450.0	446.0	166–546

Figure 3. Synthetic Case No. 1: Comparison of numerically simulated synthetic (solid lines) and available (dashed lines) GR logs (left), PEF logs (second from left), array-induction apparent resistivity logs (third from left), and neutron porosity (water-filled sandstone porosity units) and density logs (right) for the multilayer model in the water-saturated zone.

$$\rho_f = S_w \rho_w + (1 - S_w)\rho_h, \quad (4)$$

and

$$\rho_{sh} = \rho_{silt}(1 - C_{cl} - \phi_{sh}) + \rho_{cl}C_{cl} + \rho_w\phi_{sh}, \quad (5)$$

respectively, where S_w is water saturation, ϕ_{sh} is shale porosity, ρ_w is water density, ρ_h is hydrocarbon density, ρ_{cl} is clay density, ρ_{silt} is silt density, and C_{cl} is volumetric concentration of clay, defined as

$$C_{cl} = \frac{V_{cl}}{V_{sh}}, \quad (6)$$

where V_{cl} is clay volume.

Petrophysical properties of shale

Shale porosity, volumetric concentration of clay, and bound-water resistivity are necessary to estimate petrophysical properties of shaly formations. We implement the combined iterative numerical simulation of nuclear and electrical resistivity well logs specifically in pure-shale intervals to estimate shale properties. The assumptions of negligible mud-filtrate invasion, 100% volumetric concentration of shale, and 100% water saturation in shale zones reduce the nonuniqueness of the estimation. Calculated shale properties are assumed equal to those of shale encountered in nearby shaly sand intervals.

Simulation of mud-filtrate invasion

Simulation of OBM-filtrate invasion is performed with CMG (mark of Computer Modeling Group; Computer Modeling Group Ltd., 2008), a commercial reservoir simulator. We use GEM®, a compositional simulator of CMG, that numerically solves the equations of three-phase fluid flow in porous media. Developments considered in this paper assume a vertical well, horizontal layers, and axial-symmetric invasion. Inputs necessary for the numerical simulation of mud-filtrate invasion are porosity, initial fluid saturation, permeability, in situ fluid and mud properties, rock-fluid properties, and invasion parameters (including time of invasion, mud and mudcake properties, and overbalance pressure/average invasion flow rate). Numerical simulation of mud-filtrate invasion yields the postinvasion radial distribution of water saturation. Rocks are assumed water wet, whereas rock-fluid properties such as saturation-dependent capillary pressure and relative permeability are described in parametric form via Brooks-Corey's equation (Corey, 1994). Accordingly, capillary pressure is given by

$$P_c = P_c^0 \sqrt{\frac{\phi_t}{k}}(1 - S_N)^{e_p}, \quad (7)$$

where P_c is capillary pressure (MPa), P_c^0 is a constant coefficient (MPa.Darcy$^{1/2}$), ϕ_t is total porosity, k is absolute permeability (Darcy), e_p is pore-size distribution exponent, and S_N is normalized water-phase saturation, given by

$$S_N = \frac{S_w - S_{wr}}{1 - S_{wr} - S_{hr}}, \quad (8)$$

where S_{wr} is irreducible water saturation and S_{hr} is residual hydrocarbon saturation. Water and hydrocarbon saturation-dependent relative permeabilities k_{rw} and k_{rh}, respectively, are given by

$$k_{rw} = k_{rw}^0 S_N^{e_w}, \quad (9)$$

and

$$k_{rh} = k_{rh}^0 (1 - S_N)^{e_h}, \quad (10)$$

where k_{rw}^0 and k_{rh}^0 are relative permeability end points, and e_w and e_h are experimental exponents for water and hydrocarbon relative permeability, respectively. Capillary-pressure and relative-permeability parameters included in Brooks-Corey's equations are iteratively adjusted when minimizing the difference between well logs and their numerical simulations as part of the estimation method.

Table 4. Deepwater Gulf of Mexico, Field Example No. 1: Summary of assumed Archie's parameters and matrix, mud, fluid, and formation properties.

Variable	Value	Units
Archie's factor, a	1.00	–
Archie's porosity exponent, m	1.92	–
Archie's saturation exponent, n	2.00	–
Connate-water resistivity at 148°F	0.03	ohm-m
Bound-water resistivity at 148°F	0.026	ohm-m
Water density	1.00	g/cm³
Water viscosity	1.00	cp
In situ hydrocarbon density	0.10	g/cm³
Hydrocarbon viscosity	0.84	cp
Mud-filtrate density	0.77	g/cm³
Mud-filtrate viscosity	1.50	cp
Formation temperature	148.0	°F
Initial formation pressure	53.43	MPa
Mudcake reference permeability	0.03	mD
Mudcake reference porosity	0.30	–
Mud solid fraction	0.06	–
Mudcake maximum thickness	1.02	cm
Mudcake compressibility exponent	0.40	–
Mudcake exponent multiplier	0.10	–
Wellbore radius	14.94	cm
Shale porosity	0.15	–
Overbalance pressure	1.72	MPa
Formation maximum invasion time	3.0	days

Table 5. Deepwater Gulf of Mexico, Field Example No. 1: Summary of assumed rock-fluid properties for the fluid system connate water-OBM filtrate.

P_c^0 (MPa.Darcy$^{1/2}$)	e_p	k_{rw}^0	e_h	k_{rw}^0	e_w	S_{wr}	S_{hr}
0.055	7.0	0.99	4.0	0.37	4.2	0.15	0.02

We emphasize that Brooks-Corey's equation formally describes saturation-dependent properties for immiscible imbibition displacement (the wetting fluid phase displacing the nonwetting fluid phase). In the present study, OBM displaces water (wetting fluid phase), hence the immiscible fluid displacement condition is that of drainage under the assumption that the rock remains water wet after mud-filtrate invasion. We assume that Brooks-Corey's equation remains valid for drainage conditions; previous work on mud-filtrate invasion modeling indicates that this remains a good approximation (Malik et al., 2008; Salazar et al., 2011).

The initial guess for Brooks-Corey's parameters can be based on core measurements for saturation-dependent relative permeability and capillary pressure. In the absence of core measurements, water saturation estimated in the flushed zone and hydrocarbon saturation estimated in the virgin zone can be used as the initial guess for irreducible water saturation and residual hydrocarbon saturation, respectively. The latter method for choosing an initial guess is only valid in the case of OBM-invading water-saturated zones. The rest of Brooks-Corey's parameters can be chosen arbitrarily when constructing an initial guess of layer-by-layer properties.

Saturation-dependent capillary pressure

The proposed interpretation method estimates water-oil capillary pressure based on the physics of OBM-filtrate invasion within water-saturated zones. We modify the calculated radial water-OBM capillary pressure to that of water-hydrocarbon given by

$$P_{c,wg} = P_{c,wo} \frac{\gamma_{wg} \cos \theta_{wg}}{\gamma_{wo} \cos \theta_{wo}}, \quad (11)$$

where γ is interfacial tension (dynes/cm) and θ is contact angle between water and hydrocarbon phases (Purcell, 1949; Schowalter, 1979; Zinszner and Pellerin, 2007).

Saturation-dependent capillary pressure is converted to a saturation-height distribution using densities of hydrocarbon and water and the assumption of linear hydrostatic variations of pressure with depth (Schowalter, 1979; Zinszner and Pellerin, 2007), namely,

Figure 5. Synthetic Case No. 2: Sensitivity of induction apparent resistivity to permeability and porosity for the case of OBM-filtrate invasion into a water-saturated sand. Curves describe numerically simulated AIT (mark of Schlumberger) apparent resistivities (five radial lengths of investigation: R10 (shallowest), R20, R30, R60, and R90 (deepest). The permeability-to-porosity ratio is kept constant at 4 mD. Porosity ranges from 0.10 to 0.35, whereas permeability varies between 40 and 140 mD. Time of mud-filtrate invasion is three days in all cases. Table 4 lists the assumed drilling, invasion, and fluid properties.
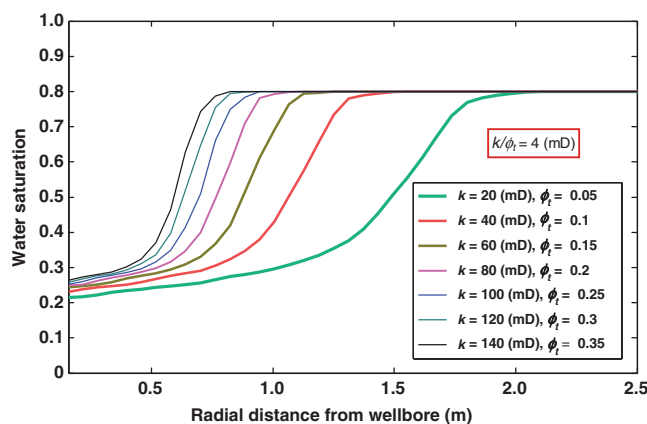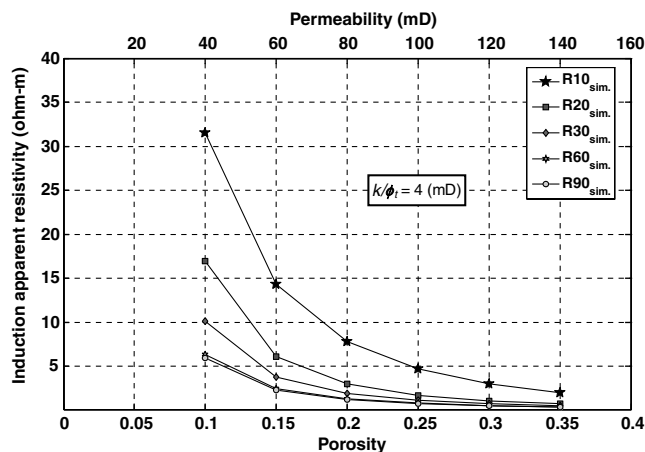

Figure 4. Synthetic Case No. 2: Sensitivity of the radial profile of water saturation to permeability and porosity. Curves describe radial distributions of water saturation resulting from OBM-filtrate invasion into different water-saturated rock types (defined with different values of porosity and permeability). The permeability-to-porosity ratio is kept constant at 4 mD. Saturation-dependent capillary pressure and relative permeability are also kept constant. Porosity ranges from 0.05 to 0.35, while permeability varies between 20 and 140 mD. Time of mud-filtrate invasion is three days in all cases. Table 4 lists the assumed drilling, invasion, and fluid properties.
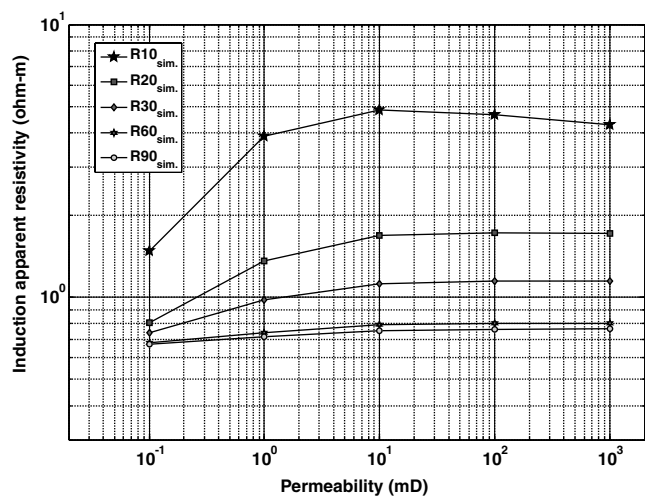

Figure 6. Synthetic Case No. 2: Sensitivity of induction apparent resistivities to permeability for the case of OBM-filtrate invasion into a water-saturated sand. Curves describe numerically simulated AIT (mark of Schlumberger) apparent resistivities (five radial lengths of investigation: R10 (shallowest), R20, R30, R60, and R90 (deepest). Permeability ranges from 0.1 to 1000 mD, whereas porosity is kept constant at 0.25. Time of mud-filtrate invasion is three days in all cases. Table 4 lists the assumed drilling, invasion, and fluid properties.

$$P_c = (\rho_w - \rho_h)gh, \qquad (12)$$

where ρ_w is water density, ρ_h is hydrocarbon density, h is height above the free water-hydrocarbon contact, and g is the gravity constant. This latter step is used for cross validation of the saturation-dependent capillary pressure estimated from the physics of OBM-filtrate invading a water-saturated rock.

Numerical simulation of well logs

The first step in the numerical simulation of well logs is to assess the radial distributions of density, migration length, PEF, electrical resistivity, and volumetric concentrations of uranium, potassium, and thorium from postinvasion radial distribution of water saturation. Density (equation 3), neutron porosity, PEF, array-induction electrical resistivity, and GR logs are numerically simulated based on those radial distributions.

We use Schlumberger's SNUPAR commercial software (McKeon and Scott, 1989) to assess migration length and PEF, from chemical compositions and their corresponding volumetric concentrations in each of the layers. Nuclear logs are thereafter simulated via fast linear iterative refinement (Mendoza et al., 2010).

The radial distribution of electrical resistivity is calculated with the dual-water, shaly sand resistivity model (Clavier et al., 1977) from the previously calculated radial distribution of water saturation. Such radial distribution is the input for numerical simulation of array-induction apparent resistivity logs (AIT, mark of Schlumberger).

Nonlinear inverse problem

In the field examples investigated in this paper, beds are usually thick (thicker than 0.61 m [2 ft]), whereby shoulder-bed effects on well logs are negligible in the center of beds. Thus, one can safely implement layer-by-layer inversion of center-bed values of well logs. Nonlinear inversion of well logs for a single layer is performed by minimizing the quadratic cost function

$$\mathbf{C(x)} = \|\mathbf{W_d} \bullet [\mathbf{d(x)} - \mathbf{d_m}]\|_2^2 + \alpha^2 \|\mathbf{x}\|_2^2, \qquad (13)$$
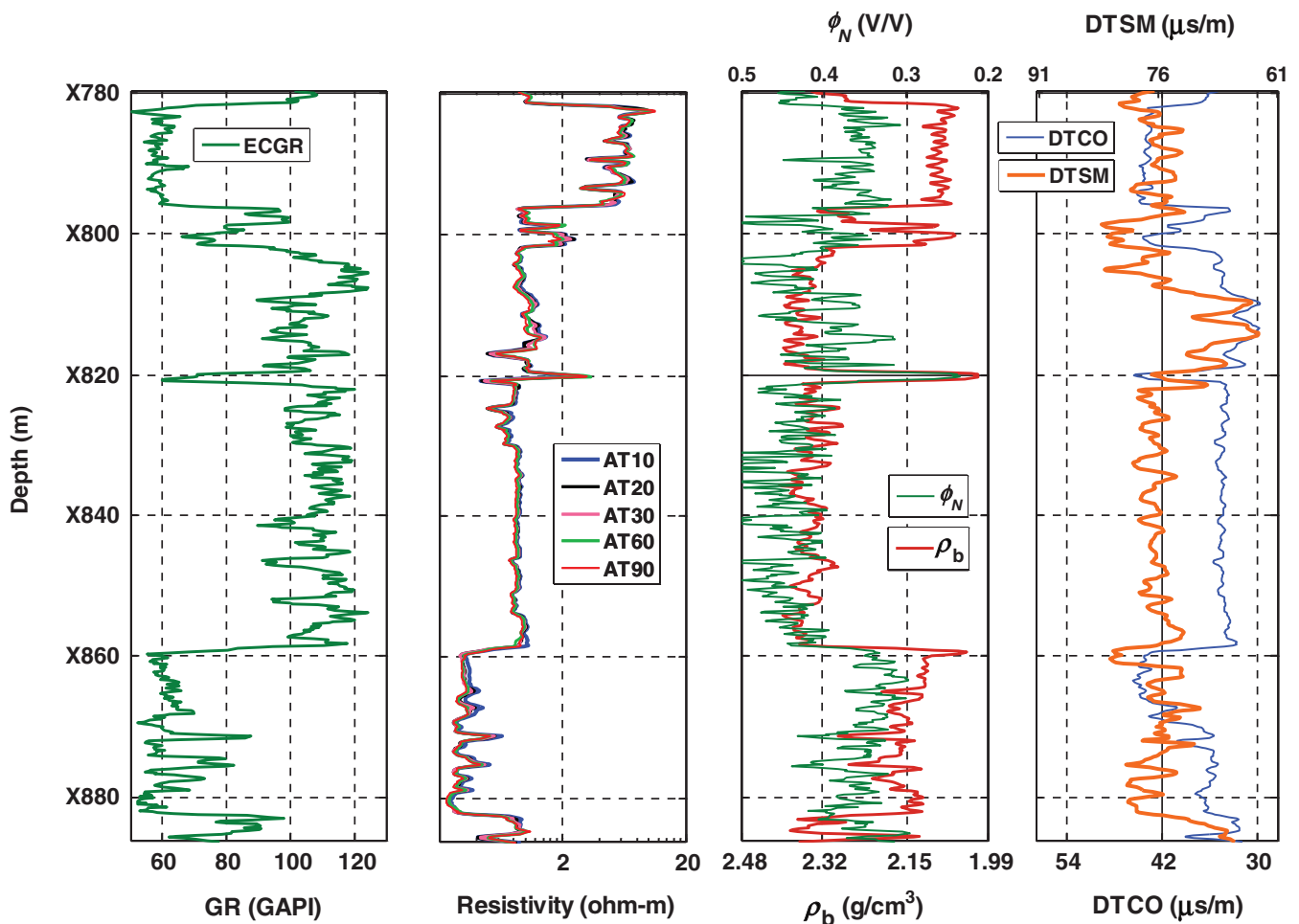
subject to

$$x_i \geq 0, \qquad (14)$$

and

Figure 7. Gulf of Mexico, Field Example No. 1: Well logs in the hydrocarbon-bearing zone underlain by a water-bearing zone located in the depth interval of X860–X882 m. Panels from left to right show GR, array-induction apparent electrical resistivity, neutron porosity and density, and shear- and compressional-wave slowness logs, respectively.
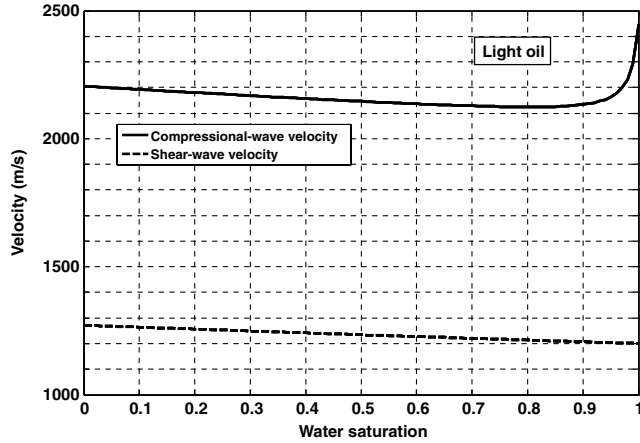
Figure 8. Field Example No. 1: Variations of compressional- and shear-wave velocity due to variations of water saturation in a rock formation containing light oil. Compressional-wave velocity exhibits a sudden increase when water saturation is higher than 0.90. This effect gives rise to a relatively large difference between compressional- and shear-wave acoustic velocities measured in the water-saturated interval.

$$C_m + C_{sh} + \phi_s = 1, \tag{15}$$

where $\mathbf{W_d}$ is a data-weighting matrix, $\mathbf{d(x)}$ is the vector of numerically simulated logs, $d_{\mathbf{m}}$ is the vector of available well logs, α is a regularization (stabilization) parameter, and $\mathbf{x}$ is the vector of unknown static/dynamic petrophysical properties. Equation 15 is valid only in the presence of dispersed shale. However, depending on the assumed rock model, it can be modified for cases of laminated or structural shale. Vector $\mathbf{x}$ can be expressed as

$$\mathbf{x} = [C_m, C_{sh}, \phi_s, S_w, S_{wr}, k, P_c^0, e_p, k_{rh}^0, e_h]^T, \tag{16}$$

where the superscript T indicates transpose and C_m is total volumetric concentration of minerals in each bed. The vector of well logs or their numerical simulation is given by

$$\mathbf{d} = [\phi_N, \rho_b, PEF, GR, \boldsymbol{\sigma}]^T, \tag{17}$$

where ϕ_N is neutron porosity and $\boldsymbol{\sigma}$ identifies all the available apparent conductivity center-bed values from each log. Apparent conductivity logs are the inverse of array-induction apparent resistivity
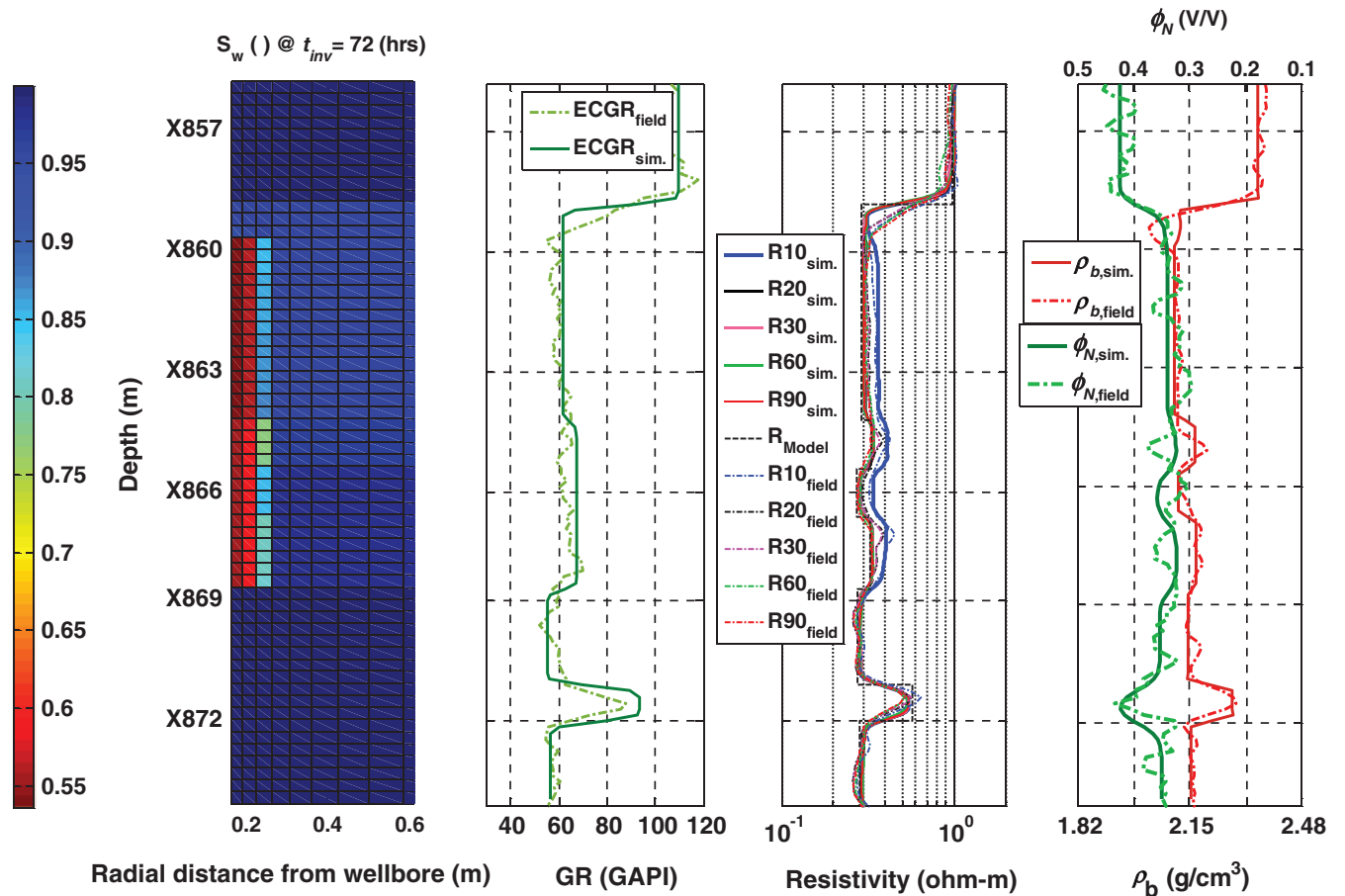

Figure 9. Deepwater Gulf of Mexico, Field Example No. 1: Comparison of numerically simulated (solid lines) and available (dashed lines) GR logs (second left panel), array-induction apparent resistivity logs (third left panel), and neutron porosity (water-filled sandstone porosity units) and density logs (right) for the multilayer model in the water-bearing zone. The left panel shows the spatial distribution (radial and vertical directions) of water saturation. Time of mud-filtrate invasion (t_{inv}) is three days. Layer-by-layer petrophysical properties were estimated by matching field logs with their numerical simulations (Table 7).

measurements and include five curves with different radial lengths of investigation ($\sigma 10$, $\sigma 20$, $\sigma 30$, $\sigma 60$, and $\sigma 90$).

The data-weighting matrix in equation 13 controls the importance of each well log included in the inversion; $\mathbf{W_d}$ is given by

$$\mathbf{W_d} = \begin{bmatrix} \frac{1}{d_{m,1}} & . & . & . & 0 \\ . & . & & & . \\ . & & . & & . \\ . & & & . & . \\ 0 & . & . & . & \frac{1}{d_{m,n_l}} \end{bmatrix}, \qquad (18)$$

where n_l is the number of well logs. Noisy or biased well logs can be eliminated from the inversion process by entering a negligible value to the corresponding entry of the data-weighting matrix.

The quadratic cost function defined in equation 13 is minimized using Levenberg-Marquardt's method (Marquardt, 1963), which is a nonlinear gradient-based technique. We calculate the entries of the Jacobian matrix numerically (finite differences) by perturbing each unknown parameter and quantifying the corresponding perturbation of every well log involved in the estimation. Based on experience, the stabilization parameter included in equation 13 is needed to approach this potentially unstable minimization problem. Such a parameter reduces nonuniqueness in the presence of noisy, inadequate, and/or incomplete data. We select the stabilization parameter with Hansen's (1994) L-curve strategy. The stabilization parameter takes a large value at the initial iterations to expedite the convergence; it gradually decreases with number of iterations to secure a stable convergence in the vicinity of the minimum of the quadratic cost function. Appendix A provides additional details about the specific approach implemented in this paper to minimize equation 13.

In the inverse problem under consideration, the number of well logs and equality constraints is usually lower than the number of unknown properties/parameters; consequently, the inversion is underdetermined. Experience shows that the simultaneous inversion to estimate all the unknown petrophysical properties and Brooks-Corey's parameters can easily become trapped in local minimums. Angeles (2009), Alpak et al. (2008), and Zeybek et al. (2004) indicated a similar challenge in their work. They claimed that results obtained using joint inversion were significantly influenced by the initial guess. Angeles (2009) introduced a method based on iterative serial inversion loops for joint inversion of formation-tester and electrical resistivity measurements to estimate Brooks-Corey's parameters. In this paper, we adopt the same approach using only apparent resistivity logs.

In the first step, we estimate porosity and volumetric concentrations of mineral constituents and shale. As long as the formations under study do not exhibit complex lithology, uncertainty in the assessment of volumetric concentration of shale and porosity will remain negligible. Next, array-induction resistivity measurements (five measurements) are used to estimate Brooks-Corey's parameters and absolute permeability in a serial inversion approach. We start the serial inversion to estimate the parameter that exhibits the maximum sensitivity to well logs. Then, we fix that parameter and estimate the next most sensitive parameter, until we estimate all the unknowns. Finally, we return to the first parameter and restart the process with the updated values for unknown properties. Figure 2 shows the different steps of the iterative serial inversion approach. Additional details about the algorithm are provided in the section entitled "Synthetic Case No. 1."

Brooks-Corey's parameters that can be reliably estimated with this method include P_c^0, e_p, S_{wr}, S_{hr}, k_{rh}^0, and e_h. Assessment of k_{rw}^0 and e_w is not reliable due to marginal sensitivity of well logs to these parameters for the case of OBM-invading water-saturated

Table 6. Deepwater Gulf of Mexico, Field Example No. 1: Averaged petrophysical properties calculated with conventional well-log interpretation.

Variable	Value	Units
Thickness	18.30 (60 ft)	m
Absolute permeability, k	100.0	mD
Nonshale porosity, ϕ_s	0.22	–
Total water saturation, S_w	1.00	–
Volumetric concentration of shale, C_{sh}	0.45	–

Table 7. Deepwater Gulf of Mexico, Field Example No. 1: Multilayer petrophysical properties obtained after matching well logs with their numerical simulations, and corresponding uncertainty range for properties estimated after perturbing well logs with zero-mean, 5% random Gaussian additive noise.

Layer thickness (m)	k (mD)	ϕ_s	C_{sh}	S_w
3.05 (10.0 ft) (Shale)	<0.001	0.00	1.00	1.00
5.49 (18.0 ft)	$50 + [-32, 150]$	0.265 ± 0.004	0.32 ± 0.012	0.96 ± 0.013
1.22 (4.0 ft)	$100 + [-48, 210]$	0.225 ± 0.00	40.42 ± 0.014	0.97 ± 0.013
1.22 (4.0 ft)	$120 + [-101, 280]$	0.255 ± 0.004	0.42 ± 0.014	0.98 ± 0.013
1.83 (6.0 ft)	$110 + [-92, 230]$	0.225 ± 0.004	0.42 ± 0.014	0.98 ± 0.013
2.44 (8.0 ft)	<0.001	0.25 ± 0.004	0.40 ± 0.014	$1.00 + [-0.016, 0]$
0.91 (3.0 ft)	<0.001	0.11 ± 0.003	0.65 ± 0.014	$1.00 + [-0.024, 0]$
2.13 (7.0 ft)	<0.001	0.245 ± 0.004	0.40 ± 0.014	$1.00 + [-0.016, 0]$

sands (however, in the case of WBM invading hydrocarbon-bearing zones, the method does yield reliable estimates of k_{rw}^0 and e_w).

In the following sections, we describe the application of the proposed interpretation method to two synthetic cases and three field examples. The three field examples are selected to cover the wide range of porosity and permeability values often encountered in siliciclastic sedimentary sequences.

SYNTHETIC CASE NO. 1: SINGLE-LAYER HYDROCARBON-BEARING FORMATION

Synthetic Case No. 1 is constructed based on petrophysical properties of a shaly sand hydrocarbon-bearing formation underlain by an active aquifer (i.e., Field Example No. 3). This synthetic example is intended to examine the sensitivity of well logs to dynamic petrophysical properties and to illustrate how the estimation procedure is implemented with fully automatic inversion. We also quantify the uncertainty of estimated properties.

The synthetic case describes a water-saturated zone invaded with OBM. Archie's parameters and matrix, mud, fluid, and formation properties assumed in Synthetic Case No. 1 are equal to those assumed for Field Example No. 3 (Table 1). Nonshale porosity, volumetric concentration of shale, and initial water saturation in the

single-layer formation are assumed equal to 0.14, 0.28, and 0.90, respectively. Table 2 lists the assumed Brooks-Corey's parameters and absolute permeability.

Well logs input to the interpretation process are GR, density, neutron porosity, PEF, and array-induction apparent resistivity. Figure 3 compares the numerically simulated logs for the single-layer synthetic case to input measurements. Because PEF and GR are primarily affected by volumetric concentration of shale in the formation, we first estimate volumetric concentration of shale based on PEF and GR. Experience shows that, in this case, the effect of dynamic petrophysical properties is lower than 0.2 water-filled sandstone porosity units and 0.005 g/cm³ on neutron porosity and density measurements, respectively. Consequently, we use density and neutron porosity logs to estimate porosity and do not include them in the inversion of Brooks-Corey's parameters and absolute permeability.

In Synthetic Case No. 1, we first investigate the sensitivity of electrical resistivity measurements to absolute permeability and Brooks-Corey's parameters separately. In the separate inversion of each parameter (assuming that the rest of the parameters are known), the final estimate converges to model values for all the parameters with relative errors lower than 0.01%. Table 2 lists
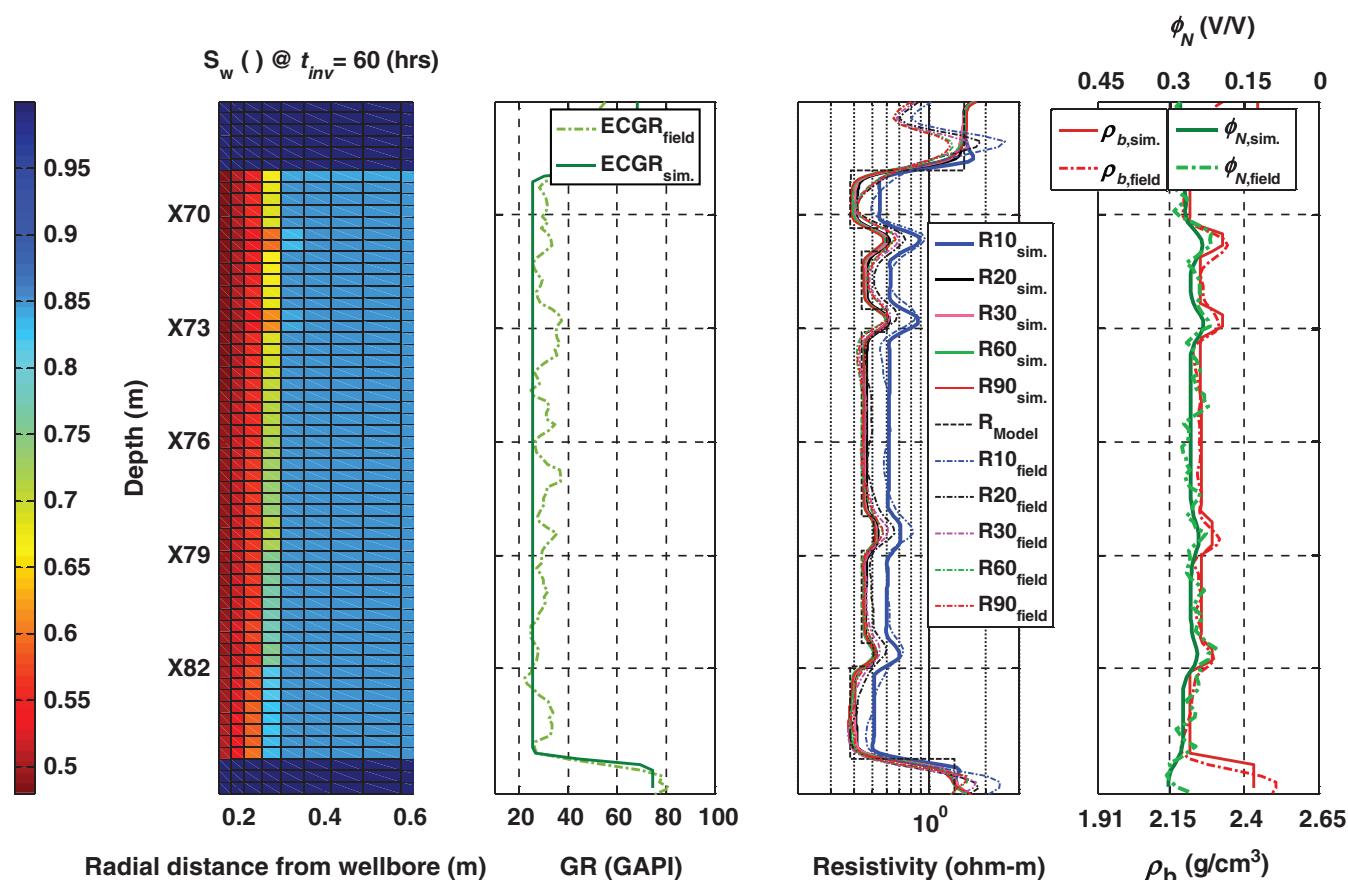

Figure 10. Central North Sea Sandstone, Field Example No. 2: Comparison of numerically simulated (solid lines) and available (dashed lines) GR logs (second panel from left), array-induction apparent resistivity logs (third panel from left), and neutron porosity (water-filled sandstone porosity units) and density logs (right) for the multilayer model in the water-bearing zone. The left panel shows the spatial distribution (radial and vertical directions) of water saturation. Time of mud-filtrate invasion (t_{inv}) is one day. Layer-by-layer petrophysical properties were estimated by matching field logs with their numerical simulations (Table 11).

model parameters, initial guess, and final estimates of permeability and Brooks-Corey's parameters. The same table describes the corresponding error ranges of final estimates obtained by perturbing array-induction apparent resistivity with zero-mean, 2% random Gaussian additive noise.

Next, we implement iterative serial inversion loops. Based on the error ranges reported in Table 2, apparent resistivity logs exhibit the maximum sensitivity to e_p and the minimum sensitivity to absolute

permeability. Consequently, the first loop starts with an inversion to estimate e_p, whereas the remaining parameters are set to their initial values. Afterward, the second inversion loop estimates P_c^0 with the updated e_p value, whereas remaining parameters are set to their initial values. We continue in the same way with the third loop to simultaneously estimate k_{rh}^0 and e_h, and thereafter with the fourth loop to estimate permeability. Next, we return to the first loop and repeat the process with updated parameters until satisfying the convergence criterion (Figure 2). The convergence criterion is either (1) relative error lower than 1% between well logs and their numerical simulations, or (2) constant error in two subsequent iterations. Table 3 describes the results obtained for Brooks-Corey's parameters and permeability after two iterations using the iterative serial

Table 8. Central North Sea Sandstone, Field Example No. 2: Summary of assumed Archie's parameters and matrix, mud, fluid, and formation properties.

Variable	Value	Units
Archie's factor, a	1.00	–
Archie's porosity exponent, m	1.89	–
Archie's saturation exponent, n	1.92	–
Connate-water resistivity at 254°F	0.025	ohm-m
Bound-water resistivity at 254°F	0.01	ohm-m
Water density	1.00	g/cm^3
Water viscosity	1.00	cp
In situ oil density	0.75	g/cm^3
Oil viscosity	1.00	cp
Mud-filtrate density	0.73	g/cm^3
Mud-filtrate viscosity	1.50	cp
Formation temperature	254.00	°F
Initial formation pressure	25.16	MPa
Mudcake reference permeability	0.03	mD
Mudcake reference porosity	0.30	–
Mud solid fraction	0.06	–
Mudcake maximum thickness	1.02	cm
Mudcake compressibility exponent	0.40	–
Mudcake exponent multiplier	0.10	–
Wellbore radius	15.24	cm
Shale porosity	0.09	–
Overbalance pressure	0.69	MPa
Formation maximum invasion time	2.50	days

Table 10. Central North Sea Sandstone, Field Example No. 2: Summary of estimated rock-fluid properties for the fluid system connate water-OBM filtrate and corresponding uncertainty range for properties estimated after perturbing well logs with zero-mean, 5% random Gaussian additive noise. Figure 11 shows the capillary pressure curve associated with these parameters.

Parameter	Final estimate	Uncertainty range
P_c^0 (MPa.Darcy$^{1/2}$)	0.062	$0.062 + [-0.032, 0.056]$
e_p	4.0	$4.00 + [-2.27, 2.74]$
k_{rh}^0	1.0	$1.00 + [-0.15, 0.00]$
e_h	7.0	$7.00 + [-1.24, 1.92]$
k_{rw}^0	0.8	$0.80 + [-0.56, 0.20]$
e_w	3.0	$3.00 + [-3.00, 4.96]$
S_{wr}	0.08	$0.080 + [0.055, 0.046]$
S_{hr}	0.15	0.15 ± 0.01
k (mD)	200.0	$200 + [-140, 640]$

Table 11. Central North Sea Sandstone, Field Example No. 2: Multilayer total porosities estimated after matching well logs with their numerical simulations, and corresponding uncertainty range estimated after perturbing well logs with zero-mean, 5% random Gaussian additive noise.

Layer thickness (m)	$\phi_{t,\text{estimated}}$	$\phi_{t,\text{core}}$
1.83 (6.0 ft) (shale)	0.09	–
1.52 (5.0 ft)	0.27 ± 0.003	0.27
0.61 (2.0 ft)	0.21 ± 0.003	0.20
1.52 (5.0 ft)	0.25 ± 0.003	0.23
0.61 (2.0 ft)	0.21 ± 0.003	0.21
4.88 (16.0 ft)	0.25 ± 0.003	0.23
0.91 (3.0 ft)	0.23 ± 0.003	0.22
2.44 (8.0 ft)	0.25 ± 0.003	0.24
0.61 (2.0 ft)	0.23 ± 0.003	0.22
2.44 (8.0 ft)	0.27 ± 0.003	0.26
0.91 (3.0 ft) (shale)	0.09	–

Table 9. Central North Sea Sandstone, Field Example No. 2: Summary of calculated average petrophysical properties calculated with conventional well-log interpretation.

Variable	Value	Units
Thickness	18.29 (60 ft)	m
Absolute permeability k	200.0	mD
Nonshale porosity ϕ_s	0.24	–
Total water saturation S_w	1.00	–
Volumetric concentration of shale C_{sh}	0.05	–

inversion approach. Although final estimates are close to actual model values, the uncertainty range is significant. Furthermore, due to nonuniqueness, final results in this case are sensitive to the initial guess. For instance, a 10% increase in the initial guess for permeability increases the error of estimated permeability by 40%.

SYNTHETIC CASE NO. 2: SENSITIVITY OF WELL LOGS TO STATIC AND DYNAMIC FORMATION PROPERTIES

Synthetic Case No. 2 is a single-layer formation constructed based on Field Example No. 1, with the same formation/fluid properties. This synthetic case is intended to examine the sensitivity of well logs to porosity and permeability. Drilling mud is OBM and the formation is saturated with water and residual hydrocarbon. Table 4 and Table 5 describe the assumed Archie's parameters and matrix, mud, fluid, and formation properties, as well as rock-fluid properties, respectively.

Sensitivity of well logs to formation properties in the presence of mud-filtrate invasion

Sensitivity of the radial profile of water saturation to porosity and permeability

The radial profile of water saturation due to invasion is controlled by formation/fluid properties and influences well logs. Figure 4 describes the effect of porosity and permeability on the radial profile of water saturation. Although the permeability-porosity ratio remains constant, the radial length of invasion decreases and the invasion front becomes piston-like with an increase of porosity and permeability. Furthermore, this example shows that the common assumption of piston-like invasion in the presence of OBM is not valid in formations with low porosity and permeability. Radially smooth variations of water saturation affect well logs and, consequently, conventional well-log interpretation. Next, we investigate the effect of this "ramp-up" radial profile of water saturation on array-induction apparent resistivity logs.
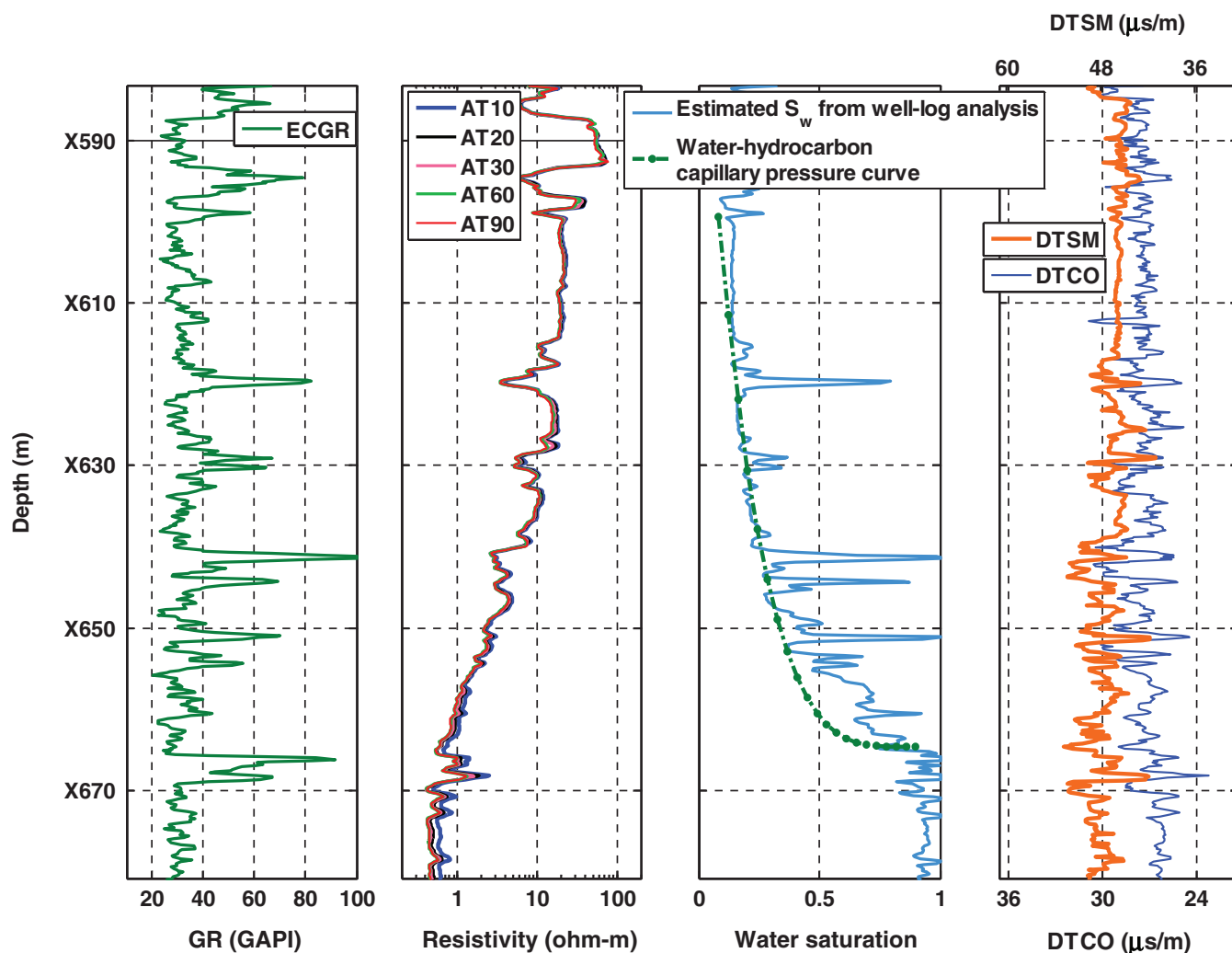

Figure 11. Central North Sea Sandstone, Field Example No. 2: Comparison of the calculated water-oil capillary pressure curve against vertical variations of water saturation calculated with petrophysical interpretation of well logs. The capillary pressure curve was obtained by matching field logs with numerical simulations. First and second left panels show GR and array-induction apparent electrical resistivity logs, respectively. The right panel shows shear- and compressional-wave slowness logs.

Sensitivity of electrical resistivity measurements to porosity and permeability

Figure 5 compares array-induction apparent resistivities for a range of permeability-porosity ratios. The maximum separation between apparent resistivity logs takes place with low permeability and porosity values where the invasion profile is radially smooth, thereby enabling the estimation of dynamic petrophysical properties.

However, separation between apparent resistivity logs is not the only requirement for accurate permeability assessment. To investigate the possibility of permeability assessment based on separation between apparent resistivity logs, we fix porosity to 0.25, vary permeability in the range from 0.1 to 1000 mD, and numerically simulate mud-filtrate invasion and the corresponding apparent resistivity logs. Figure 6 shows the sensitivity of separation between array-induction apparent resistivity logs to permeability. Although separation of apparent resistivity logs increases with an increase of permeability, for permeability values greater than 50 mD, array-induction apparent resistivities are not sensitive to permeability values any longer. This limit of sensitivity depends on the specific rock type.

FIELD EXAMPLE NO. 1: DEEPWATER GULF OF MEXICO

This field example considers a turbidite depositional sequence in the deepwater Gulf of Mexico. The reservoir mainly consists of channel levees with unconsolidated shaly sand, which can be observed in the form of massive sand and shale-laminated intervals. Rock formations contain more than 85% quartz and less than 15% clay minerals including illite/smectite, kaolinite, and chlorite (Malik et al., 2008). Porosity and permeability vary in the range from 0.20–0.34 and 10–2500 mD, respectively.

Figure 7 shows well logs across the hydrocarbon-bearing zone, underlain by an active aquifer. We observe separation of apparent resistivity logs in the water-bearing zone due to presence of OBM. A sudden separation exists between acoustic compressional- (V_P) and shear- (V_S) wave velocities in the upper section of the water-saturated zone. To explain this sudden separation of acoustic velocities, we construct a synthetic case based on fluid/formation properties and investigate the sensitivity of compressional- and shear-wave velocities to water saturation. Compressional- and shear-wave velocities are calculated using Biot-Gassmann's equations (Gassmann, 1951; Biot, 1956; Mavko et al., 2009) in a formation varying from fully hydrocarbon-saturated to fully water-saturated conditions. Figure 8 shows compressional- and shear-wave velocities as a function of water saturation. For values of water saturation higher than 0.9, a sharp increase in compressional-wave velocity causes an increase in the difference between compressional- and shear-wave velocities. This sensitivity analysis confirms that the presence of light hydrocarbon in the upper zone of the water-saturated sand is responsible for the sharp increase in compressional-wave velocity.

We focus our analysis on the water-saturated zone depicted in Figure 9. Numerically simulated logs compare well to measurements in the top and bottom shale intervals as well as across the water-saturated sand, with a relative error below 5%. Table 4 and Table 5 describe the Archie's parameters and matrix, mud, fluid, and formation properties, as well as rock-fluid properties, re-

spectively, assumed for this zone. Table 6 lists the average petrophysical properties of the water-saturated zone of interest, which are used to initialize the estimation. Based on results obtained from the estimation in the upper shale zone, shale porosity is 0.15 and clay type is assumed to be illite. Numerical simulations performed in the shale zone also estimated bound-water resistivity equal to 0.026 ohm-m at reservoir temperature. The radial length of mud-filtrate invasion is less than 0.21 m (0.7 ft), whereby the sensitivity of array-induction apparent resistivity logs to dynamic petrophysical properties is relatively low. Concomitantly, the shallow radial invasion profile makes the interpretation of neutron porosity and density logs complicated when using conventional interpretation methods because one can no longer assume that the volumes of investigation of density and neutron porosity logs are limited to the invaded zones. Thus, predicting the effect of mud-filtrate invasion on well logs in this example would be difficult without numerical simulation of the process of invasion.

Well logs used in the combined iterative simulation consist of array-induction electrical resistivity, neutron porosity, density, and GR. Table 7 describes the petrophysical properties estimated in the water-saturated zone, including nonshale porosity, absolute permeability, volumetric concentration of shale, and initial water saturation. Due to a sharp radial invasion front and the corresponding stacked array-induction apparent resistivity logs, electrical resistivity measurements exhibit marginal sensitivity to dynamic petrophysical properties. Consequently, the estimated saturation-dependent capillary pressure and relative permeability are not accurate in this case.

FIELD EXAMPLE NO. 2: CENTRAL NORTH SEA SANDSTONE

This example concerns a Paleocene sandstone dome located in the Central North Sea (Martin et al., 2005). The examined depth zone contains an oil-saturated column with a gravity of 40°API underlain by an active aquifer (BP, 2003). Rock formations chiefly consist of noncalcareous, blocky gray mudstone interbedded with sandy, high-density gravity-flow deposits and minor volcaniclastic
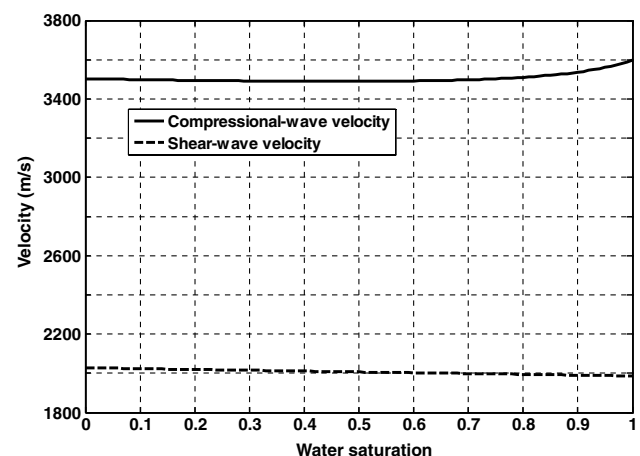

Figure 12. Central North Sea Sandstone, Field Example No. 2: Variations of compressional- and shear-wave slowness due to variations of water saturation in a rock formation containing oil. The slight decrease of compressional-wave slowness and the slight increase of shear-wave slowness in water- and hydrocarbon-bearing zones shown above are in agreement with measured logs (Figure 11).

units. Porosity varies from 0.20–0.28, wherease permeability varies from 50 to 1000 mD. Figure 10 compares well logs and their numerical simulations in the water-saturated zone. The water-saturated zone is located between two shale layers. Numerically simulated logs compare well to available logs within the two shale intervals. The combined iterative simulation of well logs yields a value of shale porosity equal to 0.09, with clay type assumed to be illite. Bound-water resistivity at reservoir temperature is 0.01 ohm-m based on simulation results. Table 8 lists the Archie's parameters and matrix, mud, fluid, and formation properties assumed for this zone. Table 9 describes average petrophysical properties in the water-saturated zone of interest, which are used as an initial guess for combined iterative simulation of well logs. Core measurements for porosity and permeability in the water-saturated zone vary between 0.21–0.25 and 200–300 mD, respectively.

Array-induction apparent resistivity, neutron porosity, density, and GR logs are input to the estimation method. Values estimated for permeability, water saturation, and volumetric concentration of shale within the examined depth interval remain approximately constant and equal to 200 mD, 0.85, and 0.05, respectively. The order

of magnitude of permeability estimates is in agreement with core measurements (in the range of 200–300 mD). Table 10 lists the estimated rock-fluid properties. Table 11 compares layer-by-layer porosity values to core measurements.

To cross validate interpretation results, Figure 11 compares the estimated capillary pressure curve against the vertical water saturation profile calculated with conventional petrophysical interpretation of well logs. This exercise indicates an agreement in trend and value between the water-hydrocarbon capillary pressure and the radial water saturation profile within the water-saturated sand invaded with OBM. The right-most track in Figure 11 shows an increase in shear-wave slowness and a decrease in compressional-wave slowness between hydrocarbon- and water-bearing zones. Results from Biot-Gassmann's fluid substitution, shown in Figure 12, are in agreement with measured compressional- and shear- wave slowness in water- and hydrocarbon-bearing zones.

FIELD EXAMPLE NO. 3: TRINIDAD SHALY SAND

This field example considers a Trinidad shaly sand sequence located within a delta sedimentary system (Liu, 2007). Our analysis
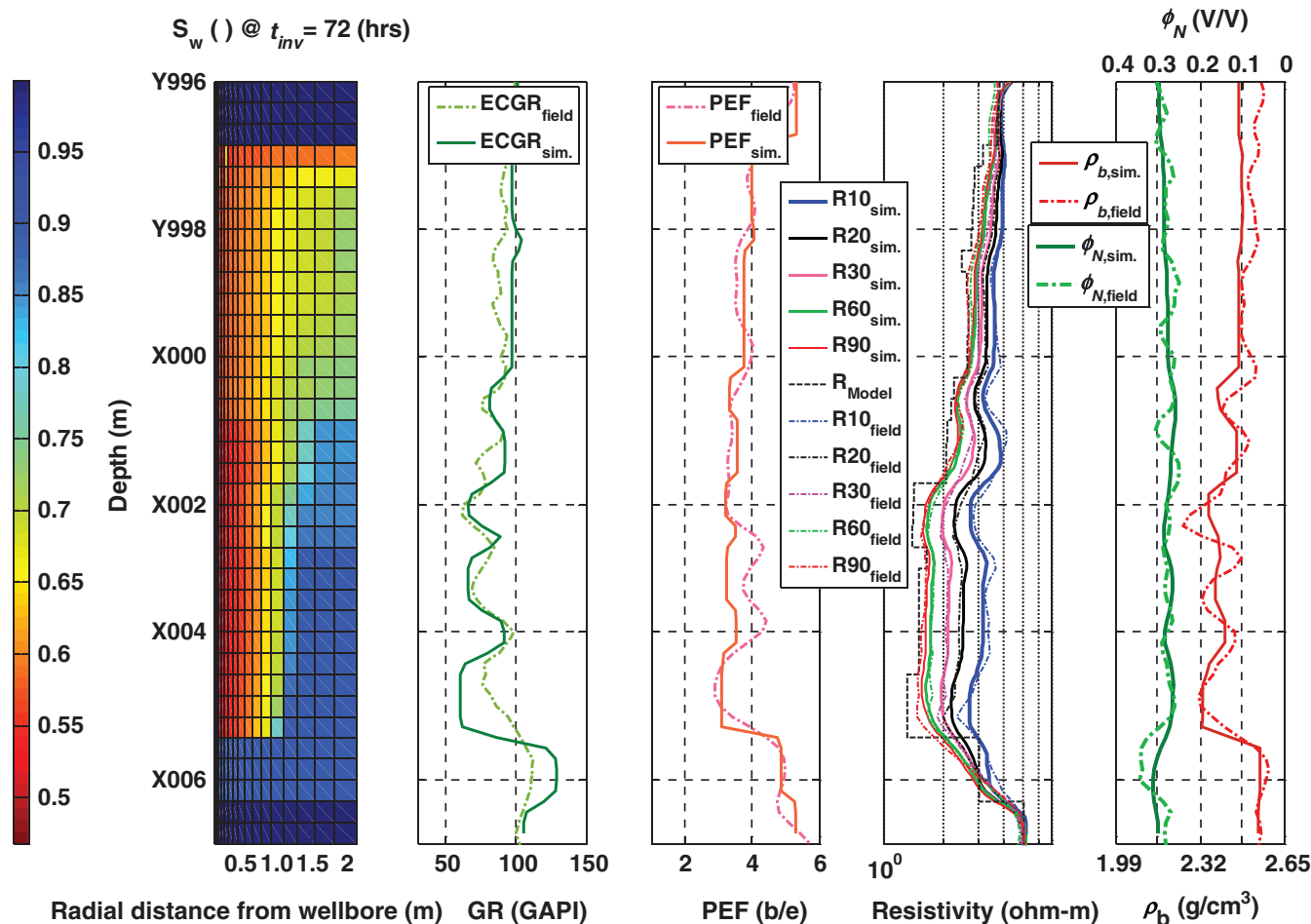

Figure 13. Trinidad Shaly Sand, Field Example No. 3: Comparison of numerically simulated (solid lines) and available (dashed lines) GR logs (second panel from left), PEF logs (third panel from left), array-induction apparent resistivity logs (fourth panel from left), and neutron porosity (water-filled sandstone porosity units) and density logs (right panel) for the multilayer model in the water-bearing zone. The left panel shows the spatial distribution (radial and vertical directions) of water saturation. Time of mud-filtrate invasion (t_{inv}) is three days. Petrophysical properties were obtained by matching field logs with their numerical simulations (Table 14).

is focused to a gas-bearing zone located above an aquifer invaded with OBM. Average porosity and permeability in the zone of interest are 0.14 and 500 mD, respectively.

Figure 13 shows well logs and their numerical simulations across the water-bearing zone. Table 1 summarizes Archie's parameters and matrix, mud, fluid, and formation properties assumed for this zone. Shale porosity was estimated at 0.10 based on the combined iterative simulation of well logs with the assumption of illite as the dominant clay type. Bound-water resistivity was also estimated to be 0.03 ohm-m at reservoir temperature. Table 12 lists the average petrophysical properties for the simulation interval; the same values are used as initial guess for the iterative combined simulation of well logs.

We use array-induction apparent resistivity, neutron porosity, density, PEF, and GR logs for the combined iterative simulation of well logs. Table 13 and Table 14 document the estimated values of Brooks-Corey's parameters and nonshale porosity, water saturation, volumetric concentration of shale, and permeability within the water-saturated zone, respectively.

Figure 14 compares the estimated saturation-dependent water-gas capillary pressure against the vertical water saturation profile calculated with conventional well-log interpretation. A good agreement is observed between water-gas capillary pressure and the vertical distribution of water saturation, which verifies the results obtained with the proposed interpretation method. To assess saturation-dependent water-gas capillary pressure, we first estimate water-oil capillary pressure via combined iterative numerical simulation of well logs. Subsequently, saturation-dependent water-gas capillary pressure is estimated based on water-oil capillary pressure (equation 11).

DISCUSSION

This paper proposes a method to estimate dynamic (e.g., absolute permeability and saturation-dependent capillary pressure and relative permeability) and static (e.g., porosity and water saturation) petrophysical properties based on combined numerical simulation

Table 12. Trinidad Shaly Sand, Field Example No. 3: Summary of average petrophysical properties calculated with conventional well-log interpretation.

Variable	Value	Units
Thickness	10.97 (36 ft)	m
Absolute permeability k	500.0	mD
Nonshale porosity ϕ_s	0.14	–
Total water saturation S_w	1.00	–
Volumetric concentration of shale C_{sh}	0.45	–

Table 13. Trinidad Shaly Sand, Field Example No. 3: Summary of estimated rock-fluid properties for the fluid system connate water-OBM filtrate and corresponding uncertainty range for properties estimated after perturbing well logs with zero-mean, 5% random Gaussian additive noise. Figure 14 shows the capillary pressure curve associated with these parameters.

Parameter	Final estimate	Uncertainty range
P_c^0 (MPa.Darcy$^{1/2}$)	0.186	$0.186 + [-0.030, 0.120]$
e_p	5.0	$5.0 + [-0.7, 0.8]$
k_{rh}^0	0.7	$0.7 + [-0.4, 0.3]$
e_h	2.5	$2.5 + [-0.8, 1.1]$
k_{rw}^0	0.6	$0.6 + [-0.5, 0.4]$
e_w	4.5	$4.5 + [-1.5, 10.6]$
S_{wr}	0.15	0.15 ± 0.07
S_{hr}	0.10	0.10 ± 0.02

Table 14. Trinidad Shaly Sand, Field Example No. 3: Multilayer petrophysical properties obtained after matching well logs with numerical simulations, and corresponding uncertainty range for properties estimated after perturbing well logs with zero-mean, 5% random Gaussian additive noise.

Layer thickness (m)	k (mD)	ϕ_s	C_{sh}	S_w
0.91 (3.0 ft) (shale)	<0.001	0.00	1.00	1.00
1.52 (5.0 ft)	$700 + [-590, 130]$	0.10 ± 0.002	0.38 ± 0.009	0.75 ± 0.015
1.83 (6.0 ft)	$700 + [-580, 140]$	0.11 ± 0.002	0.32 ± 0.008	0.78 ± 0.015
0.61 (2.0 ft)	$700 + [-590, 170]$	0.125 ± 0.003	0.28 ± 0.008	0.65 ± 0.012
0.91 (3.0 ft)	$400 + [-330, 410]$	0.115 ± 0.002	0.28 ± 0.008	0.85 ± 0.014
0.91 (3.0 ft)	$400 + [-340, 500]$	0.155 ± 0.003	0.28 ± 0.008	0.85 ± 0.012
0.30 (1.0 ft)	$3350 + [-2220, 6940]$	0.13 ± 0.003	0.28 ± 0.008	0.90 ± 0.014
1.83 (6.0 ft)	$3350 + [-2240, 6500]$	0.14 ± 0.003	0.28 ± 0.008	0.90 ± 0.014
0.91 (3.0 ft)	$400 + [-350, 490]$	0.155 ± 0.003	0.28 ± 0.008	0.90 ± 0.014
0.91 (3.0 ft)	0.001	0.05 ± 0.002	0.52 ± 0.010	0.90 ± 0.030
0.61 (2.0 ft) (shale)	<0.001	0.00	1.00	1.00

and inversion of nuclear and resistivity logs. We focused our study to water-saturated sands and shaly sands invaded with OBM. In such cases, (1) separation between array-induction apparent resistivity logs is not negligible and, consequently, the sensitivity of resistivity logs to dynamic properties is measurable, (2) mud filtrate and connate water are immiscible, and (3) salt mixing between mud filtrate and connate water is negligible. The latter conditions included in the estimation method partially eliminate the effect of uncertainty associated with invasion parameters on inversion results. We also applied the proposed method to pure shale zones to estimate shale properties such as shale porosity and bound-water resistivity. We then used these properties in shaly sand zones to reduce nonuniqueness of inversion results.

Data and parameters input to the inversion are the following: (1) well logs, including array-induction apparent resistivity/conductivity logs with different radial lengths of investigation (five radial lengths of investigation), neutron porosity, density, GR, and PEF, (2) invasion properties such as time of invasion, overbalance pressure, and mud/mud-cake properties, (3) formation and fluid properties such as mineralogy of the formation and density, viscos-

ity, and chemical formula of in situ fluids, (4) bed-boundary locations, (5) a saturation-porosity-resistivity model and associated parameters (e.g., the dual water model and its associate parameters such as connate-water and bound-water resistivity, constants, porosity exponent, and saturation exponent), and (6) a saturation-dependent capillary pressure and relative permeability model (e.g., Brooks-Corey's model). Uncertainty in any of the input data/parameters affects the final estimates of static and dynamic petrophysical properties. However, inaccuracies in the location of bed boundaries and matrix composition were not significant concerns in this study because all the field examples considered siliciclastic sequences with beds thicker than 0.61 m (2 ft) with no complex lithology.

To define the range of reliability of the proposed estimation method in the assessment of porosity, absolute permeability, and Brooks-Corey's parameters, we quantified the sensitivity of well logs to those properties by performing random zero-mean perturbations of the input well logs. Estimated properties from the highest to lowest reliability were porosity, volumetric concentration of shale, initial water saturation, irreducible water saturation (S_{wr}), pore-size
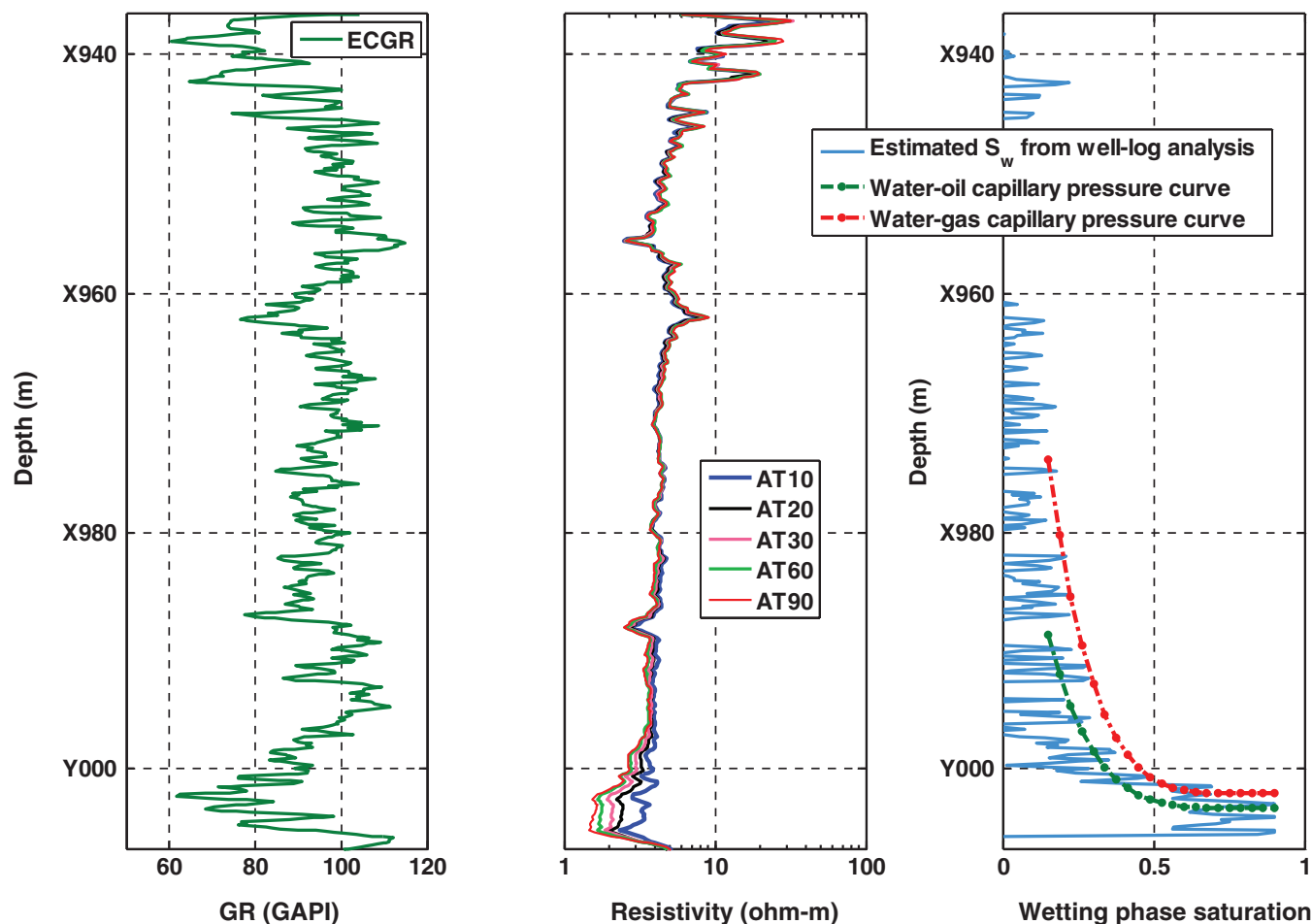

Figure 14. Trinidad Shaly Sand, Field Example No. 3: Comparison of calculated water-oil capillary pressure curve and corresponding water-gas capillary pressure curve against vertical variations of water saturation calculated with petrophysical interpretation of well logs (right panel). Capillary pressure curves were obtained by matching field logs with numerical simulations. Left and center panels show GR and array-induction apparent resistivity logs, respectively.

distribution exponent (e_p), coefficient for capillary pressure equation (P_c^0), hydrocarbon-phase exponent for Brooks-Corey's equation (e_h), end point of hydrocarbon-phase relative permeability (k_{rh}^0), and permeability. The sensitivity of well logs to the end point of water-phase relative permeability (k_{rw}^0) and water-phase exponent for Brooks-Corey's equation (e_w) was marginal in the presence of OBM invading water-saturated sand zones. Consequently, the introduced method was not reliable in the assessment of k_{rw}^0 and e_w.

Assessment of dynamic petrophysical properties with the proposed estimation method is reliable when the separation between apparent resistivity logs is not negligible. The sensitivity of the inversion method to dynamic petrophysical properties become marginal in the presence of (1) stacked electrical resistivity logs, (2) shallow radial length of invasion (shallower than 0.15 m [0.5 ft]), and (3) very deep radial length of invasion (deeper than 2.44 m [8 ft]). Among the three field examples investigated in this paper, Field Example No. 1 exhibited the shallowest radial length of invasion, where the separation among array-induction apparent resistivity logs was negligible. Consequently, the proposed estimation method was not reliable in the assessment of dynamic petrophysical properties. For the remaining field examples, comparison of the estimated saturation-dependent capillary pressure against the vertical distribution of water saturation in the reservoir confirmed the reliability of the proposed method in assessing capillary pressure.

In all the synthetic cases and field examples studied in this paper, the number of well logs was lower than the number of unknown petrophysical properties, leading to an underdetermined inversion. In such cases, nonuniqueness of results was a major concern. Furthermore, including additional well logs in the estimation did not always reduce the nonuniqueness of results, especially when the well logs did not exhibit sensitivity to dynamic petrophysical properties (e.g., PEF and GR). We found that the simultaneous inversion of well logs could become trapped in local minimums due to nonuniqueness. To circumvent this problem, we implemented an iterative serial inversion approach to estimate permeability and Brooks-Corey's parameters. Although such an approach provided accurate results for Synthetic Case No. 1, estimation results were still sensitive to the initial guess. To achieve the most accurate results in those cases, the initial guess should be chosen close to actual values. Core data are the best choice for the initial guess. In the absence of core data, the initial guess for porosity, volumetric concentration of shale, permeability, irreducible water saturation, and initial water saturation could be obtained from conventional petrophysical interpretation. A parsimonious initial guess could be used for the rest of Brooks-Corey's parameters.

CONCLUSIONS

We introduced a new method to estimate dynamic petrophysical properties of water-bearing rocks invaded with OBM. The method honors the physics of fluid flow in porous and permeable media and takes advantage of the immiscibility between mud filtrate and connate water. Furthermore, it quantitatively combines electrical resistivity, density, neutron porosity, PEF, and GR logs, explicitly takes into account the differences in volumes of investigation of the various measurement instruments involved, and consistently reduces nonuniqueness in the estimation.

The estimation method was successfully tested on three field examples and two synthetic cases constructed from actual field examples. Field examples considered siliciclastic hydrocarbon-bearing reservoirs underlain by active aquifers and covered a wide range of porosity and permeability values to investigate the reliability and accuracy of the estimation method. Comparison of saturation-dependent capillary pressure in the water-bearing zones to the estimated radial profile of water saturation confirmed the accuracy and reliability of the estimation method. We also showed that the inferred radial profile of water saturation enables the numerical simulation of borehole acoustic logs (compressional- and shear-wave velocity logs) via fluid-substitution equations to match available well logs.

The introduced method to estimate dynamic petrophysical properties is best suited for those cases where the radial profile of water saturation resulting from invasion is smooth, and the separation between apparent resistivity logs is not negligible. It was found that the accuracy of estimated properties decreased in the presence of shallow invasion and/or sharp radial profiles of water saturation. Likewise, the method is not sensitive to dynamic petrophysical properties in cases of radially deep mud-filtrate invasion. In general, any property that decreases the separation of array-induction resistivity logs (e.g., presence of fresh connate water in the OBM-invaded formation) will decrease the sensitivity of measurements to dynamic petrophysical properties.

Even though the introduced interpretation method could be applied to cases of WBM or OBM invading water- or hydrocarbon-bearing zones, the specific situation where OBM invades water-saturated zones gives rise to maximum sensitivity of apparent resistivity logs to formation properties. However, in the cases of OBM invading water-saturated zones, estimates of end point and exponent for Brooks-Corey's equation for water-phase relative permeability are not reliable. We recommend this method for assessment of static and dynamic petrophysical properties in field examples where (a) electrical resistivity measurements with different radial lengths of investigation are available and (b) the separation between electrical resistivity logs is not negligible.

NOMENCLATURE

a	=	Archie's factor
C_m	=	Volumetric concentration of minerals
C_{sh}	=	Volumetric concentration of shale
$\mathbf{C(x)}$	=	Cost function
$\mathbf{d}$	=	Vector of numerically simulated well logs
$\boldsymbol{d_m}$	=	Vector of measured or modeled well logs
e_p	=	Pore-size distribution exponent
e_h	=	Hydrocarbon-phase experimental exponent for Brooks-Corey's equation
e_w	=	Water-phase experimental exponent for Brooks-Corey's equation
g	=	Gravity constant (m/s^2)
h	=	Height above the free water-hydrocarbon contact (m)
k	=	Absolute permeability (mD)
k_{rh}	=	Hydrocarbon-phase relative permeability
k_{rh}^0	=	k_{rh} end point
k_{rw}^0	=	k_{rw} end point
k_{rw}	=	Water-phase relative permeability
m	=	Archie's porosity exponent
n	=	Archie's saturation exponent
n_l	=	Number of well logs
n_{sp}	=	Number of sampling points for each well log

P_c = Capillary pressure (MPa)
P_c^0 = Coefficient for P_c equation (MPa.Darcy$^{1/2}$)
R = Apparent resistivity measurements (ohm-m)
S_{hr} = Residual hydrocarbon saturation
S_N = Normalized water-phase saturation
S_w = Total water saturation
S_{wr} = Irreducible water saturation
t_{inv} = Time of mud-filtrate invasion (hours, days)
V_m = Matrix volume (m^3)
V_p = Acoustic compressional-wave velocity (m/s)
V_{ps} = Pore-space volume (m^3)
V_s = Acoustic shear-wave velocity (m/s)
V_{sh} = Shale volume (m^3)
$\mathbf{W_d}$ = Data-weighting matrix
α = Regularization parameter
ϕ_N = Neutron porosity
ϕ_{sh} = Shale porosity
ϕ_s = Nonshale porosity
ϕ_t = Total porosity
ρ_b = Bulk density (g/cm^3)
ρ_h = Hydrocarbon density (g/cm^3)
ρ_w = Water density (g/cm^3)
σ = Electrical conductivity (S/m)
γ = Interfacial tension between water and hydrocarbon phases (dynes/cm)
θ = Contact angle between water and hydrocarbon phases (degree)

ACRONYMS

AIT® = Array-induction tool
CMG = Computer Modeling Group, Ltd.
DTCO = Delta-T compressional
DTSM = Delta-T shear
ECGR = Environmentally corrected gamma ray
GEM® = Compositional simulator from CMG
GR = Gamma ray
kppm = Kilo parts per million
OBM = Oil-base mud
PEF = Photoelectric factor
SNUPAR = Schlumberger nuclear parameter code
WBM = Water-base mud
3D = Three-dimensional

ACKNOWLEDGMENTS

APPENDIX A

DEFINITION OF UNKNOWN PARAMETERS ESTIMATED WITH JOINT INVERSION OF WELL LOGS

To effectively enforce the constraints expressed in equations 14 and 15, we invoke volumes/weights instead of volumetric/weight concentrations of minerals, shale, and fluids. Additionally, expressing the unknown properties in terms of their logarithmic values explicitly enforces nonnegativity of results in the estimation. Consequently, we transform the unknown variable vector $\mathbf{x}$ to a vector $\mathbf{x}'$ given by

$$\mathbf{x}' = [\log V_m, \log V_{sh}, \log V_{ps}, \log S_w, \log S_{wr}, \log k, \log P_c^0,$$
$$\log e_p, \log k_{rh}^0, \log e_h]^T, \tag{A-1}$$

where V_m is matrix volume, V_{ps} is pore-space volume, V_{sh} is shale volume, S_w is total water saturation, S_{wr} is irreducible water saturation, k is absolute permeability (Darcy), P_c^0 is a constant coefficient (MPa.Darcy$^{1/2}$), e_p is pore-size distribution exponent, k_{rh}^0 is hydrocarbon relative permeability end point, and e_h is experimental exponents for hydrocarbon relative permeability. The relationships between volumes and volumetric concentrations of minerals, shale, and fluids are given by

$$C_m = \frac{V_m}{V_m + V_{sh} + V_{ps}}, \tag{A-2}$$

$$C_{sh} = \frac{V_{sh}}{V_m + V_{sh} + V_{ps}}, \tag{A-3}$$

and

$$\phi_s = \frac{V_{ps}}{V_m + V_{sh} + V_{ps}}, \tag{A-4}$$

where C_m is volumetric concentration of the minerals (except minerals included in shale), ϕ_s is nonshale porosity, and C_{sh} is volumetric concentration of shale.

REFERENCES

Alpak, F. O., C. Torres-Verdín, T. M. Habashy, and K. Sepehrnoori, 2008, Estimation of in situ petrophysical properties from wireline formation tester and induction logging measurements: A joint inversion approach: Journal of Petroleum Science and Engineering, **63**, no. 1–4, 1–17, doi: 10.1016/j.petrol.2008.05.007.

Angeles Boza, R. M., 2009, Simulation and interpretation of formation-tester measurements acquired in the presence of mud-filtrate invasion, multiphase flow, and deviated wellbores: Ph.D. dissertation, The University of Texas at Austin.

Biot, M. A., 1956, Theory of propagation of elastic waves in a fluid saturated porous solid. I. Low frequency range and II. Higher-frequency range: Journal of the Acoustical Society of America, **28**, 168–191, doi: 10.1121/1.1908239.

BP Exploration, 2003, The UK upstream asset portfolio, BP Exploration, Farburn Industrial Estate, Dyce, Aberdeen, U.K.

Clavier, C., G. Coates, and J. Dumanoir, 1977, The theoretical and experimental bases for the dual water model for the interpretation of shaly sands: Proceedings of the AIME Annual Technical Conference and Exhibition, Society of Petroleum Engineers, SPE 6859.

Computer Modeling Group Ltd., 2008, User's guide: STARS: Computer Modeling Group Ltd.

Corey, A. T., 1994, Mechanics of immiscible fluids in porous media: Water Resources Publications.

Gassmann, F., 1951, Über die elastizitätporösermedien: Vierteljahrsschrift der NaturforschendenGesellschaft in Zürich, **96**, 1–23.

Hansen, P. C., 1994, Regularization tools: A Matlab package for analysis and solution of discrete ill-posed problems: Numerical Algorithms, **6**, no. 1, 1–35, doi: 10.1007/BF02149761.

Heidari, Z., C. Torres-Verdín, A. Mendoza, and G. L. Wang, 2011, Assessment of residual hydrocarbon saturation with the combined quantitative interpretation of resistivity and nuclear logs: Petrophysics, **52**, 217–237.

Liu, Z., 2007, Joint inversion of density and resistivity logs for the improved petrophysical assessment of thinly-bedded clastic rock formations: M.S. thesis, The University of Texas at Austin.

Malik, M., J. M. Salazar, C. Torres-Verdín, G. L. Wang, H. J. Lee, and K. Sepehrnoori, 2008, Effects of petrophysical properties on array-induction measurements acquired in the presence of oil-base mud-filtrate invasion: Petrophysics, **49**, 74–92.

Marquardt, D. W., 1963, An algorithm for least-squares estimation of nonlinear parameters: Journal of the Society for Industrial and Applied Mathematics, **11**, no. 2, 431–441, doi: 10.1137/0111030.

Martin, A. J., D. Robertson, J. Wreford, and A. Lindsay, 2005, High-accuracy oriented perforating extends the sand-free production life of Andrew field: Proceedings of the SPE at Offshore Europe, Society of Petroleum Engineers, SPE 93639.

Mavko, G., T. Mukerji, and J. Dvorkin, 2009, The rock physics handbook: Tools for seismic analysis of porous media: Cambridge University Press.

McKeon, D. C., and H. D. Scott, 1989, SNUPAR — A nuclear parameter code for nuclear geophysics applications: IEEE Transactions on Nuclear Geoscience, **36**, no. 1, 1215–1219, doi: 10.1109/23.34634.

Mendoza, A., C. Torres-Verdín, and W. E. Preeg, 2010, Linear iterative refinement method for the rapid simulation of borehole nuclear measurements, Part I: Vertical wells: Geophysics, **75**, no. 1, E9–E29, doi: 10.1190/1.3267877.

Mezzatesta, A. G., F. E. Mendez, E. F. Rodriguez, and D. Georgi, 2006, A novel approach to numerical simulation of conventional, multicomponent induction, and magnetic resonance data in shaly-sand and carbonate systems: 47th Annual Logging Symposium, SPWLA, paper GGG.

Pickett, G. R., 1966, A review of current techniques for determination of water saturation from logs: Journal of Petroleum Technology, **18**, 1425–1433, doi: 10.2118/1446-PA.

Poupon, A. C., J. Dumanoir, R. Gaymard, and A. Misk, 1970, Log analysis of sand-shale sequences: A systematic approach: Journal of Petroleum Technology, **22**, 867–881, doi: 10.2118/2897-PA.

Purcell, W. R., 1949, Capillary pressures — their measurement using mercury and the calculation of permeability therefrom: Journal of Petroleum Technology, **1**, 39–48, doi: 10.2118/949039-G.

Salazar, J. M., C. Torres-Verdín, F. O. Alpak, T. M. Habashy, and J. D. Klein, 2006, Estimation of permeability from array induction measurements: Applications to the petrophysical assessment of tight-gas sands: Petrophysics, **47**, 527–544.

Salazar, J. M., C. Torres-Verdín, and G. L. Wang, 2011, Effects of surfactant-emulsified oil-based mud on borehole resistivity measurements: SPE Journal, **16**, 608–624, doi: 10.2118/109946-PA.

Schowalter, T. T., 1979, Mechanics of secondary hydrocarbon migration and entrapment: The American Association of Petroleum Geologists Bulletin, **7**, no. 5, 723–760.

Timur, A., 1968, An investigation of permeability, porosity, and residual water saturation relationship for sandstone reservoirs: The Log Analyst, **9**, no. 4, 8–17.

Zeybek, M., T. S. Ramakrishnan, S. S. Al-Otaibi, S. P. Salamy, and F. J. Kuchuk, 2004, Estimating multiphase-flow properties from dual-packer formation-tester interval tests and openhole array resistivity measurements: SPE Reservoir Evaluation and Engineering, **7**, no. 1, 40–46, doi: 10.2118/87474-PA.

Zinszner, B., and F. M. Pellerin, 2007, A geoscientist's guide to petrophysics: Editions Technip.